nature communications

Article

https://doi.org/10.1038/s41467-025-65715-x

Achieving high-efficiency and stable refrigeration performance through composition modulation inducing non-twinned martensite

Received: 4 March 2025

Accepted: 21 October 2025

Published online: 27 November 2025

Check for updates

Jiahe Mei[1,2,3], Fei Xiao[1,2,3], Lipeng Guo[1,2,3], Xinyu Qing[1,2,3], Laisen Wang[1,3], Xingjun Liu[4], Cuiping Wang[1,3] ✉ & Shuiyuan Yang[1,2,3] ✉

The development of high-efficiency, eco-friendly, and compact refrigeration systems requires materials that achieve the ideal elastocaloric effect with minimal driving forces. However, existing shape memory alloys for refrigeration have difficulties in overcoming the trade-off between strain-dissipation work and driving force-COP_{mat} (coefficient of performance). Here, we report a Cu-18Zn-8Al-0.3V-0.3Si single-crystal alloy with a recoverable strain of 13% and a low stress hysteresis of 8 MPa under a minimal driving force of 251.1 MPa. Moreover, the alloy exhibits a high COPmat value of 17.4, with a stability over 800 cycles. The high performance is attributed to the unique microstructure of ordered domains and distortion regions induced by composition modulation, which enables simultaneous achievement of low driving force and energy dissipation during phase transformation. Additionally, the formation of non-twinned martensite contributes to maintaining long-term performance stability. This microstructure regulation strategy synergistically optimizes energy efficiency and durability, offering an innovative solution for new-generation refrigeration systems.

Billions of space cooling systems have long relied on traditional vapor compression refrigeration technology, which utilizes chlorofluorocarbons and hydrochlorofluorocarbons as refrigerants. These substances are responsible for approximately 10% of global greenhouse gas emissions, comprising indirect emissions from the cooling process and direct emissions from refrigerant leaks[1,2]. This contributes significantly to environmental degradation and exacerbates global warming. The resulting rise in temperatures, in turn, drives increased global cooling demand, creating a vicious cycle. Consequently, there is an urgent need to seek environmentally friendly alternative cooling technologies. To date, solid-state cooling technology that harnesses the elastic caloric effect (eCE) generated by stress-induced phase transitions in shape memory alloys (SMAs) has shown significant potential in terms of environmental friendliness, cooling performance, and energy efficiency.

The coefficient of performance of the material (COP_{mat}) is a key metric for assessing the eCE potential of materials, used to evaluate the cooling efficiency of different refrigeration materials. It can be expressed as the ratio of cooling capacity Q to dissipated work ΔW, where Q is proportional to the absolute value of adiabatic temperature change (ΔT_{ad}), and ΔW corresponds to the area of the stress-strain hysteresis loop[3,4]. Currently, developing SMAs with high COP_{mat} values

[1]College of Materials of Xiamen University, Xiamen, China. [2]Shenzhen Research Institute of Xiamen University, Shenzhen, China. [3]Fujian Key Laboratory of Surface and Interface Engineering for High Performance Materials, Xiamen Key Laboratory of High Performance Metals and Materials, Xiamen University, Xiamen, China. [4]Institute of Materials Genome and Big Data, Harbin Institute of Technology University, Shenzhen, PR China. ✉e-mail: wangcp@xmu.edu.cn; yangshuiyuan@xmu.edu.cn

remains a technical challenge. This is because, to achieve a substantial eCE, SMAs must undergo sufficient strain to fully induce the martensitic transformation. However, as the strain increases, the hysteresis observed in the first-order martensitic transformation process also intensifies, resulting in a greater amount of dissipated work, as shown in Fig. 1a. The stress hysteresis of SMAs is something that must be considered when repeatedly actively driving and applying energy conversion, and it is key to achieving high energy conversion efficiency and low fatigue[5]. However, this hysteresis behavior is common in SMAs across different systems, leading to an inevitable trade-off between recoverable strain and dissipated work. Therefore, this trade-off has become a key issue that needs to be overcome in the research and application of SMAs in the field of elastocaloric refrigeration.

In the past, significant research has been invested in developing NiTi/NiMnGa-SMA alloys that strike a balance between the ΔT_{ad} and ΔW, resulting in elastocaloric refrigeration SMAs with impressive COP_{mat} values that surpass 10[6–8]. By adjusting the composition and structure, a series of NiTi-SMAs with quasi-linear behavior have even been successfully designed, which are characterized by a maximum ΔW in the range of 1–2 MJ/m^3 [9–11]. However, these optimized SMAs not only come with additional production costs but also necessitate the utilization of a high driving force (exceeding 600 MPa) for actuation. This implies that in practical applications, complex, bulky, and power-hungry drivers must be employed. Consequently, a high driving force implies elevated costs and diminished efficiency. In the current pursuit of compact design, high safety, and energy efficiency in commercial refrigeration systems, existing SMAs face new challenges, the trade-off between low driving forces and high COP_{mat}, as shown in the Ashby map in Fig. 1b. It is evident that enhancing COP_{mat}, reducing driving forces, and stress hysteresis are critical pathways to stand out among various elastocaloric materials.

Here, we find that the Cu-18Zn-8Al-0.3V-0.3Si single-crystal alloy exhibits a low stress hysteresis of 8 MPa, a recoverable strain of 13%, a low driving force of 251.1 MPa, and a high COP_{mat} value of 17.4, overcoming the trade-offs between strain-dissipated work and driving force-COP_{mat}. Moreover, the alloy achieves maximum positive and negative ΔT_{ad} of 5.4 K and 5.1 K, respectively, and maintains a stable eCE of 5.1 K without degradation after 800 cycles under 7% strain. This makes its prospects for commercial application in the field of elastocaloric refrigeration much broader.

Results

Mechanical properties

The superelastic behavior of traditional alloys often exhibits a significant increase in dissipated energy as the recoverable strain increases, whereas the Cu-18Zn-8Al-0.3V-0.3Si single-crystal alloy

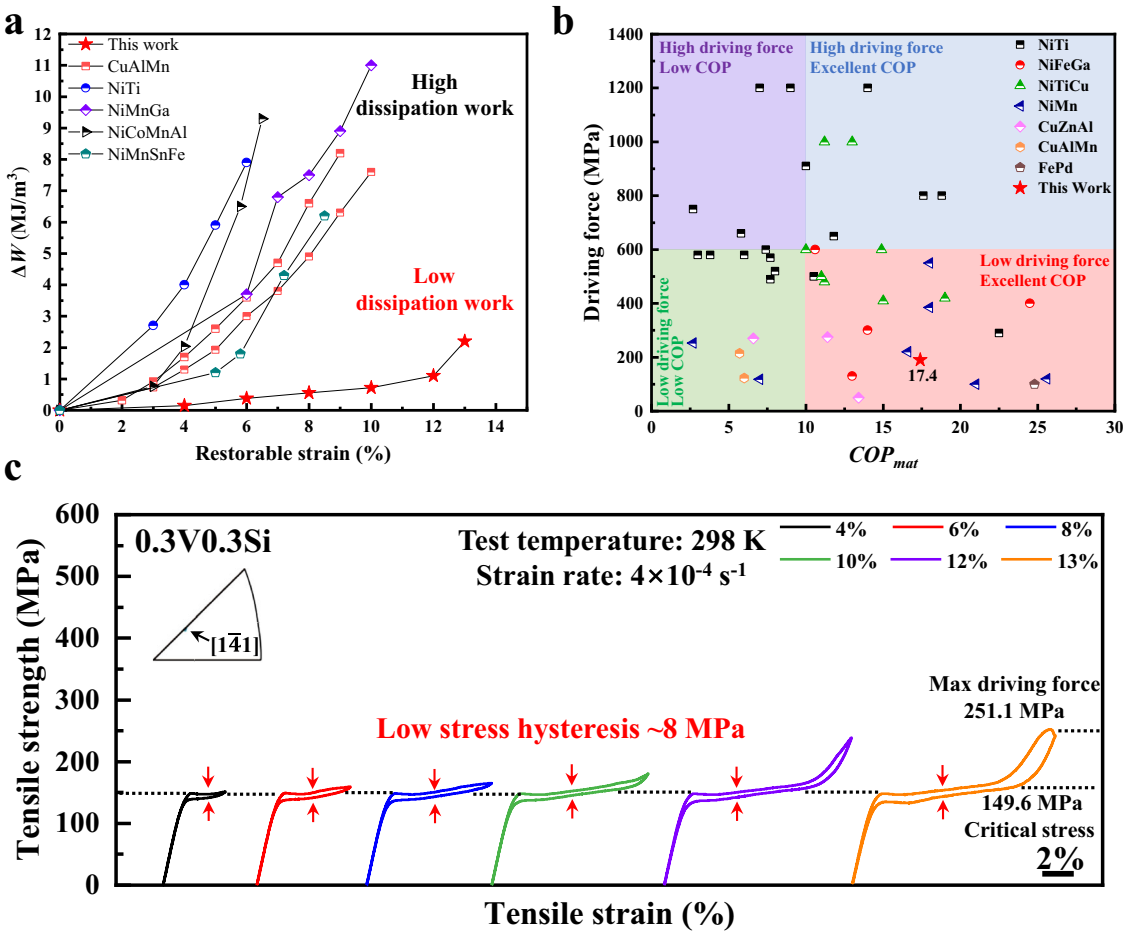

Fig. 1 | Low driving force and dissipated work elastocaloric refrigeration materials. a Comparison of the dissipated work and recoverable strain between Cu-18Zn-8Al-0.3V-0.3Si single-crystal alloy and other SMAs[19–24]. **b** Cu-18Zn-8Al-0.3V-0.3Si single-crystal alloy, with its COP_{mat} value and significant maximum driving force, achieves ultra-high refrigeration efficiency that surpasses that of existing elasto-thermal refrigeration materials. NiTi-SMAs[6,7,10,21,25–34]:, NiFeGa-SMAs[35–38]:, NiTiCu-SMAs[6,26,39–44]:, NiMn-SMAs[8,36,45–47]:, CuZnAl-SMAs[48,49]:,CuAlMn-SMAs[50,51]:, FePd-SMAs[52]:. **c** The room temperature superelastic behavior of Cu-18Zn-8Al-0.3V-0.3Si single-crystal alloy. The inset illustrates the single-crystal orientation of the alloy. Source data are provided as a Source data file.

requires no trade-off between recoverable strain and dissipated work, as shown in Fig. 1a. It achieves an impressive 13% recoverable strain with a low dissipated energy of only 2.2 MJ/m^3. This distinctive combination of properties enables the material to exhibit both substantial superelasticity and prolonged durability in elastomeric applications. On the other hand, the Cu-18Zn-8Al-0.3V-0.3Si single-crystal alloy, with only a driving force of 251.1 MPa, achieves an impressive COP_{mat} value of 17.4 (Fig. 1b), endowing it with a high cooling efficiency and energy efficiency ratio.

Figure 1c shows that the Cu-18Zn-8Al-0.3V-0.3Si single-crystal alloy demonstrates a platform-like, low stress hysteresis stress-strain curve. The alloy has a low critical stress of 149.6 MPa and a recoverable strain of 13%. The loading-unloading curve shows that its stress platform is only about 8 MPa, and the maximum driving force at the elastic limit is also just 251.1 MPa. It is worth noting that the Cu-18Zn-8Al-0.3V-0.3Si single-crystal alloy not only successfully avoids the significant hysteresis issues commonly found in traditional SMAs[12,13] but also overcomes the limitations of some existing SMAs with quasi-linear behavior that rely on high driving forces (often greater than 1 GPa) to achieve narrow hysteresis[14–16]. The Cu-18Zn-8Al-0.3V-0.3Si single-crystal alloy ingeniously integrates their advantages, achieving low hysteresis with large recoverable strain while maintaining a stable low driving force, significantly enhancing the material's practicality and efficiency.

Function and structural stability

Figure 2a demonstrates the eCE of the Cu-18Zn-8Al-0.3V-0.3Si single-crystal alloy within the strain range of 3–11%. At 11% strain, the directly measured positive and negative ΔT_{ad} attain maximum values of 5.4 K and 5.1 K, respectively. Achieving the ideal eCE with low driving force is not enough; it is essential to further ensure the structural and functional stability of the Cu-18Zn-8Al-0.3V-0.3Si single-crystal alloy for long-term applications. As shown in the stress-strain response during rapid loading/unloading in Fig. S1a, stress hysteresis exhibits only a slight increase but maintaining low levels, suggesting considerable cyclic stability. We have observed that the elastic behavior of the Cu-18Zn-8Al-0.3V-0.3Si single-crystal alloy remains stable after undergoing a large tensile strain of 8% and 200 cycles, as shown in Fig. 2b. Simultaneously, the eCE stability testing of the Cu-18Zn-8Al-0.3V-0.3Si single-crystal alloy under adiabatic conditions revealed a stable cooling capacity even after 200 cycles (Fig. S1b, c), ultimately yielding a COP_{mat} value as high as 17.4. Even after 800 consecutive rapid unloading processes (Omitting the hold time, Fig. 2c), the eCE performance (5.1 K) remains stable without any signs of degradation. This is in stark contrast to the current Cu-based elastic cooling materials, whose functionality significantly declines after just a few dozen cycles[17]. It is defined as $COP_{mat} = \frac{Q}{\Delta W} = \frac{|\Delta T_{ad} \times C_p \times \rho|}{\oint \sigma d\varepsilon}$, where Q is proportional to the absolute value of the product of the adiabatic temperature (ΔT_{ad}), the specific heat (C_p), and the density (ρ), and ΔW is the dissipated work calculated by integrating the superelastic hysteresis loop ($\oint \sigma d\varepsilon$). Since rapid loading/unloading better reflects practical refrigeration scenarios, we evaluated the Cu-18Zn-8Al-0.3V-0.3Si alloy at 7% strain (corresponding to Fig. 2c, d), with the corresponding ΔT_{ad}, $\rho \oint \sigma d\varepsilon$ and C_p values of 5.1 K, 7700 kg/m^3, 801 kJ/m^3 (800 th), and 0.43 kJ/kg·K, respectively. The COP_{mat} value of 21.1 (Omitting the hold time) was obtained for the Cu-18Zn-8Al-0.3V-0.3Si single-crystal alloy when the holding time was omitted. It is noteworthy that under high strain rates (0.1 s^{-1}), the dissipated energy and critical stress of the Cu-18Zn-8Al-0.3V-0.3Si single-crystal alloy gradually decrease with the increase in the number of cycles (Fig. 2d, e), which may be the result of the accumulation of dislocations[18]. The accumulation of dislocations and residual martensite typically during the cycling process leads to irreversible recovery in traditional SMAs, but for the Cu-18Zn-8Al-0.3V-0.3Si single crystal alloy, it can still achieve stable superelasticity and eCE.

Microstructure

The martensitic transformation temperature of the Cu-18Zn-8Al-0.3V-0.3Si single-crystal alloy is 138.9 K, in which showing a body-centered cubic D03 parent phase structure at room temperature (Fig. S2). The Cu-18Zn-8Al-0.3V-0.3Si single-crystal alloy mainly consists of extensive distortion regions, ordered domains (accounting for about 16%, with an average size of approximately 32 nm), and sporadic V_3Si particles, as shown in Fig. S3a. The distorted regions and ordered domains are the outcomes of compositional modulation, with the Zn concentration being slightly higher in the ordered domains, as shown in Fig. S3b. The high-resolution TEM (HRTEM) image of the distortion regions and ordered domains is presented in Fig. 3a. The near-spherical ordered domains, highlighted with yellow lines, correspond to the superlattice spots revealed by the Fast Fourier Transform (FFT) results in the inset. The ordered domains and V_3Si particles (Fig. S3c) both exhibit smooth interfaces with the distortion regions, without significant lattice distortion. In contrast, there is a notable presence of lattice distortion within the distortion region itself. The long-period stacking order (LPSO) structures are extensively distributed within the distortion region, with closely packed planes following the stacking sequence of AB′C/B′CA′/CA′B/A′BC′/BC′A/C′AB′/A, corresponding to the 18 R structure as shown in Fig. 3b. According to geometric phase analysis (GPA), the abundance of 18R-LPSO structures within the distortion regions has been identified as the primary source of lattice distortion, serving as favorable sites for the nucleation of martensite.

Through Atom Probe Tomography (APT) measurements, the elemental distribution in the Cu-18Zn-8Al-0.3V-0.3Si single-crystal alloy was analyzed and visualized at a three-dimensional atomic resolution, as shown in Fig. 4a. As illustrated in Fig. 4b, the compositional fluctuations in the specific region reveal the phenomenon of co-segregation of V and Si. Concurrently, Zn and Al exhibit pronounced synchronous fluctuations, with Zn displaying more pronounced variations. Moreover, the concentration changes of Cu are found to be inversely correlated with those of the aforementioned elements. The isosurfaces of Zn (22.61 at.%), V (0.28 at.%), and Si (0.28 at.%) concentrations are clearly visualized, revealing that the V-rich and Si-rich regions overlap, as shown in Fig. 4c.

Notably, a marked increase in Zn concentration is observed surrounding the V- and Si-enriched clusters. This suggests that V and Si effectively enhance the local solid solubility of Zn within the matrix, thereby inducing the formation of numerous finely dispersed ordered domains. The results obtained from APT are in agreement with those from TEM (Fig. S3), indicating that the ordered domains have higher concentrations of Zn and slightly lower concentrations of Cu compared to the distortion regions. In summary, the three-dimensional APT results further confirm that the distinct structures of the distortion regions and ordered domains are caused by compositional modulation.

As shown in Fig. 5a, b, following the stress-induced martensitic transformation, the Cu-18Zn-8Al-0.3V-0.3Si single-crystal alloy has developed a unique structure composed of dispersed single martensitic laths (with an average length of about 110 nm and an average width of approximately 4 nm) and non-twinned martensite. The results of the FFT revealed that both exhibited additional spots, corresponding to the orthorhombic 18 R martensitic structure. The difference lies in that the single martensitic lath shows a long-period

https://doi.org/10.1038/s41467-025-65715-x

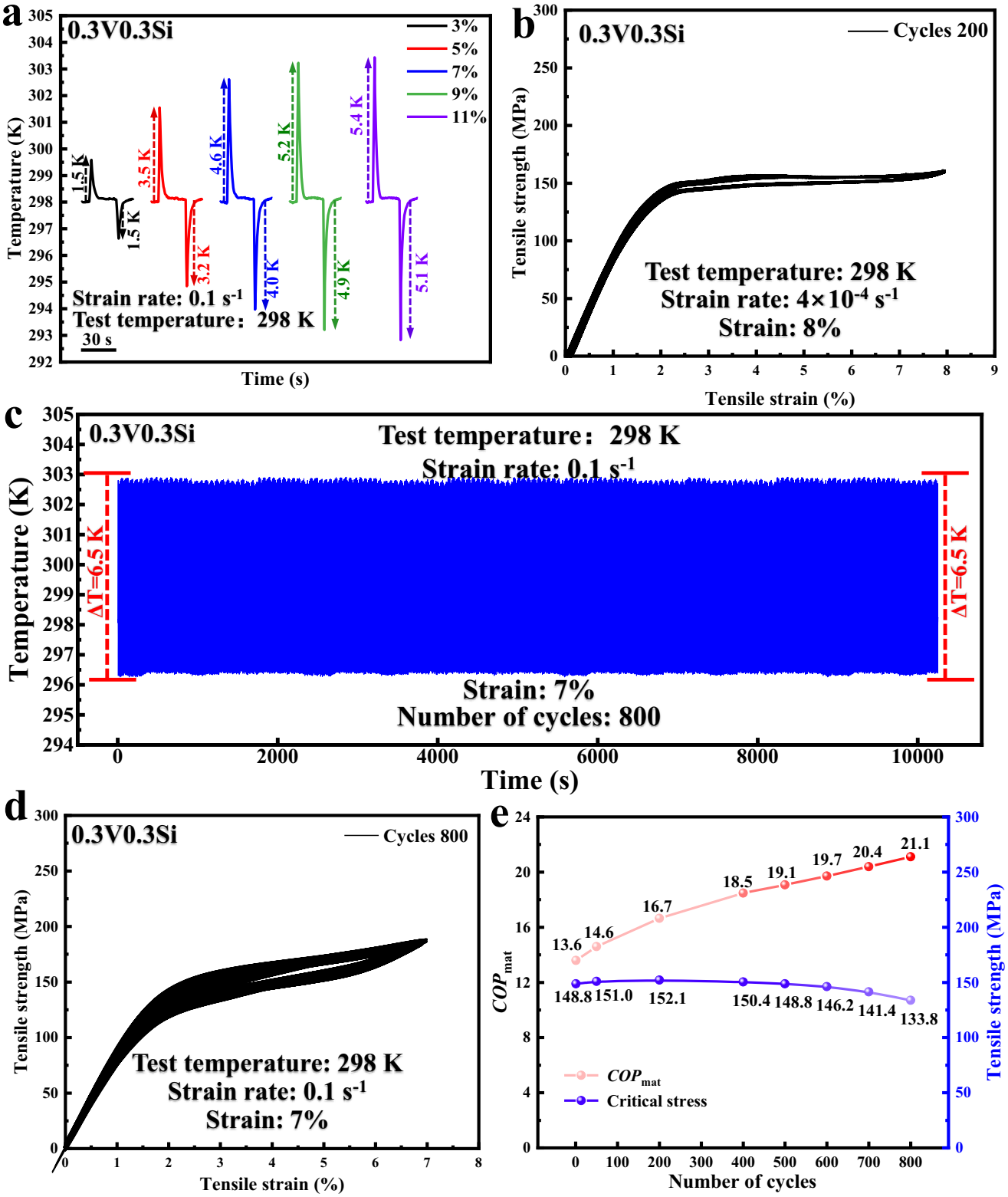

Fig. 2 | Stable structural and functional stability. a The ΔT_{ad} curves for 0.1 s^{-1} rate at different strains. **b** Cyclic tensile loading/unloading tests at 8% strain and a strain rate of 4×10^{-4} s^{-1}. **c** ΔT_{ad} curve of cyclic tensile loading/unloading tests. The 800-cycle results were obtained using the following: loading (0.1 s^{-1})−unloading (0.1 s^{-1}) −hold (10 s). This cyclic process weakens the holding time between loading and unloading, resulting in a failure to accurately measure negative ΔT_{ad}, but maximally demonstrates stable refrigeration performance. Fig. S1b reflects the true refrigeration capacity of the alloy during cycling. **d** Cyclic tensile loading/unloading tests (Omitting the hold time) at 7% strain and a strain rate of 0.1 s^{-1}. **e** The variation of COP_{mat} and critical stress with the number of cycles. Source data are provided as a Source data file.

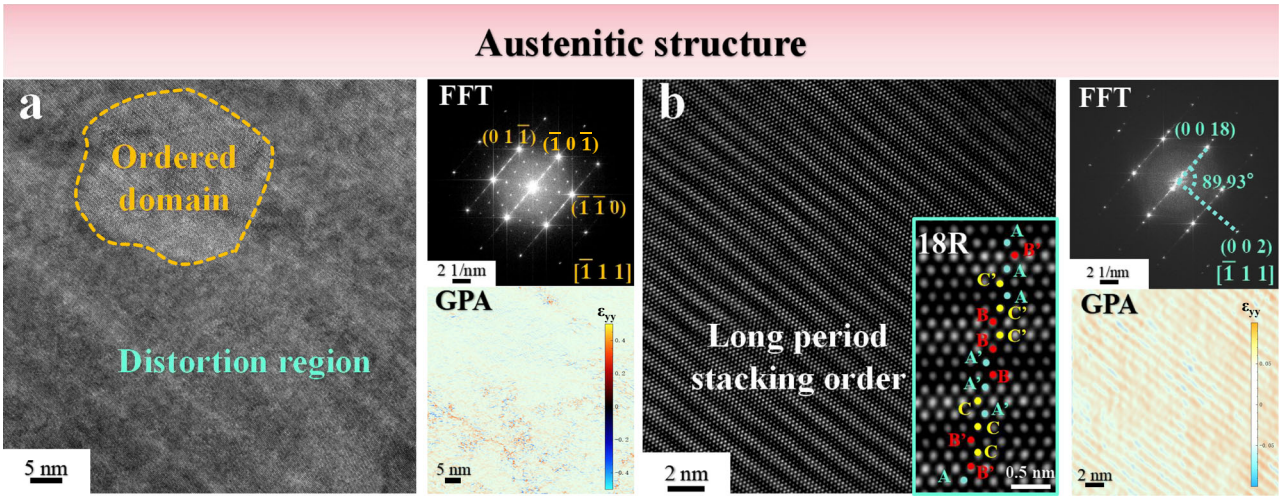

Fig. 3 | Microstructure of the matrix. a HRTEM image of Cu-18Zn-8Al-0.3V-0.3Si single-crystal alloy before deformation. The inset shows the corresponding selected area electron diffraction (SAED) and Geometric Phase Analysis (GPA) results. **b** HRTEM image of the 18R-LPSO structures within the distortion regions. The IFFT result shown in the illustration clearly reveals the periodic stacking of the 18 R structure. To further confirm its crystal structure, the corresponding FFT analysis displays an interaxial angle of 89.93°. The GPA result indicates the presence of significant lattice distortion in this structural region.

stacking characteristic (Fig. 5c), while the non-twinned martensite exhibits a shorter-period stacking (Fig. 5d), as shown in the FFT results of the corresponding region. The orderliness of the parent phase significantly affects the atomic displacement during the phase transformation, and the resulting martensite will inherit the orderliness of the parent phase. Consequently, the formation of single martensite laths and non-twinned martensite originates from the ordered domains and distortion regions of the matrix, respectively. As shown in the FFT and GPA results of Fig. 5e, f, there is a slight deviation in the diffraction spots between the single martensite lath and the non-twinned martensite, indicating a slight lattice distortion at their interfaces. Furthermore, these widely distributed non-twinned martensite have the same substructure and orientation, sharing identical crystallographic characteristics and microstructural features, and can be considered as the same variant. This implies that they follow the same transformation mechanism during their formation process.

Discussion

Microstructural evolution and transformation thermodynamics

The Cu-18Zn-8Al-0.3V-0.3Si single-crystal alloy demonstrates high efficiency and stable refrigeration capabilities, which can be attributed to its unique microstructure composed of near-spherical ordered domains and distortion regions (Figs. 3a and 6a). Doping with V/Si can induce significant compositional modulation, and the precise adjustment of their content is a crucial method for achieving the unique microstructure mentioned above. The impact of V and Si content on the evolution of the microstructure is depicted in Fig. 6.

The impact of Si content on phase transition temperature is weak. When the Si content is increased to 0.5 wt%, the M_s decreases slightly to 135.5 K (Fig. S2). The Cu-18Zn-8Al-0.3V-0.5Si single-crystal alloy also consists of ordered domains and distortion regions at room temperature, as shown in Figs. 6b and S1. The distortion regions still contain 18R-LPSO structures (Fig. S4c). Notably, increased Si content significantly enriches these near-spherical ordered domains (Fig. S4b). The size of V_3Si particles also increases substantially. V_3Si particles in the Cu-18Zn-8Al-0.3V-0.5Si alloy are significantly larger than those commonly found in the Cu-18Zn-8Al-0.3V-0.3Si alloy (~36 nm, labeled in Fig. S4a), as shown in Fig. R4d. Conversely, the content of V has a significant impact on the phase transition temperature. When the content of V is increased to 0.5 wt%, the M_s significantly increases to 191.4 K (Fig. S2). When the V content increases to 0.5 wt%, M_s significantly rises to 191.4 K. Additionally, the increase in V content leads to the transformation of the dispersed, near-spherical ordered domains into a stream-like, densely distributed ordered domains (Figs. 6c and S6). In conclusion, the augmentation of Si and V content predominantly enhances local ordering, resulting in the enrichment of ordered domains. Moreover, V exerts a more pronounced effect on compositional modulation, which significantly alters the shape of the ordered domains. The influence on the distortion regions is negligible; the pervasive distortions remain conducive to the nucleation of martensite. Notably, increases in both vanadium and silicon content lead to varying degrees of reduction in latent heat ($\Delta H_{A\text{-}M}$) during austenite-to-martensite transformation. Thus, the Cu-18Zn-8Al-0.3V-0.5Si and Cu-18Zn-8Al-0.5V-0.3Si single-crystal alloys exhibit varying degrees of weakened eCE compared to the Cu-18Zn-8Al-0.3V-0.3Si single-crystal alloy (Figs. 2a and S5c and S7c).

Stress-induced martensitic transformation

The Cu-18Zn-8Al-0.3V-0.3Si, Cu-18Zn-8Al-0.3V-0.5Si, and Cu-18Zn-8Al-0.5V-0.3Si, were found to exhibit [$\bar{1}$41], [$\bar{2}$32], and [$\bar{1}$10] orientations, respectively, as shown in Figs. 1a and S4a and S6a. Therefore, the observed differences in critical stress and stress hysteresis between samples are attributed to the combined effects of orientation differences and microstructural variations. Among these factors, the pronounced microstructural differences are identified as the primary influencing factor. Given that the single-crystal alloys were obtained through abnormal grain growth, controlling their orientation is inherently challenging. Thus, this study focuses on elucidating the relationship between the unique microstructure and SIMT.

During the stress loading-unloading cycling process, the Cu-18Zn-8Al-0.3V-0.3Si single-crystal alloy exhibits unique reversible transformation characteristics, namely between the ordered domains and the martensitic lath, as well as between the distortion regions and the non-twinned martensite (Figs. 5a and 6a1). During the stress-induced martensitic transformation, single martensite laths predominantly form in a dispersed manner, become dominantly martensite (Fig. 5a). Furthermore, the distortion regions rich in 18R-LPSO structure not only significantly reduce the nucleation barrier but also provide a multitude of favorable nucleation sites (Fig. 6a1), promoting the growth of martensite involving only short-range migration of phase boundaries. This markedly decreases the energy expenditure associated with

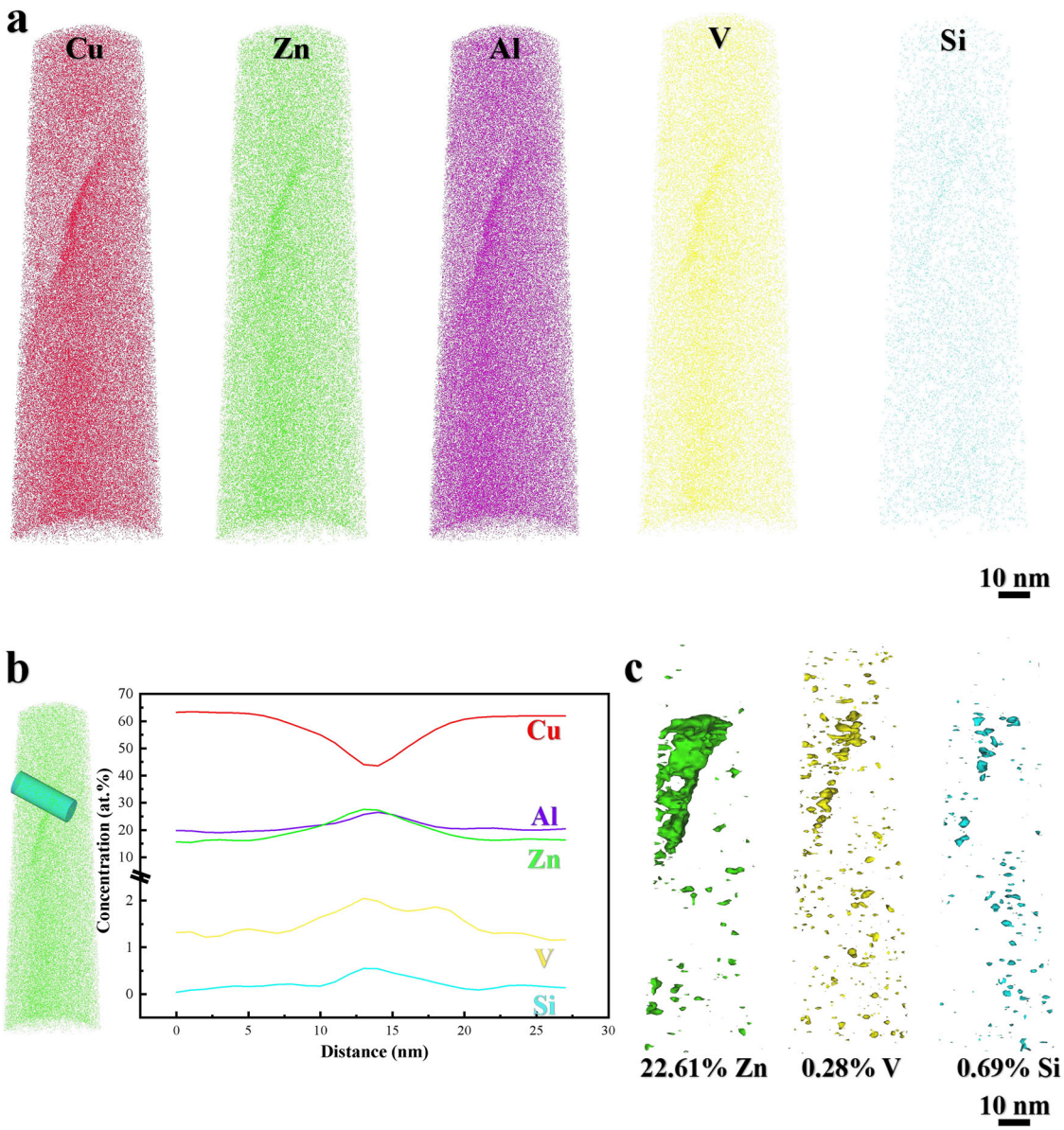

Fig. 4 | Reconstruction of the structure of the Cu-18Zn-8Al-0.3V-0.3Si single-crystal alloy. a Show the reconstruction map of all elements. **b** The compositional distribution along the cylindrical region. **c** 22.61 at.% Zn, 0.28 at.% V and 0.69 at.% Si iso-concentration surfaces. Source data are provided as a Source data file.

nucleation events and phase boundary migration during repeated cycles of loading and unloading. Furthermore, due to martensite nucleation and growth are confined to a very small region, they exhibit a strong selectivity for variants and display a pronounced crystallographic preference for the surrounding single martensitic laths, facilitating the formation of a special type of non-twinned martensite (Fig. 6a2). This non-twinned martensite can avoid the self-accommodation effects among martensite variants and reduce the formation and propagation of twins, thereby significantly reducing the resistance and additional energy consumption during the phase transformation process. As a result, Cu-18Zn-8Al-0.3V-0.3Si single-crystal alloy achieves a combination of low driving force and low dissipated work.

The Cu-18Zn-8Al-0.3V-0.3Si single-crystal alloy exhibits consistent superelastic behavior under low strain frequency cycling (Fig. 2b). Even under high strain frequency cycling, the slight accumulation of dislocations at the interface of martensitic laths leads to a minor reduction in critical stress and stress hysteresis (Fig. 2d). However, this does not result in the formation of irreversible residual martensite. Consequently, its superelasticity and elastocaloric performance remain remarkably stable.

However, the enrichment of ordered domains leads to the aggregation of single martensitic laths after transformation, which in turn significantly increases the critical stress (Cu-18Zn-8Al-0.3V-0.5Si single-crystal alloy, Figs. 6a1 and S5a). Despite the presence of non-twinned martensite reducing energy dissipation, the enrichment of martensitic lath intensifies the accumulation of dislocations during cyclic loading (Fig. 6a2). After just 200 cycles, there is a noticeable decrease in critical stress (Fig. S5b). Moreover, the Cu-18Zn-8Al-0.3V-0.5Si single-crystal alloy exhibits a mediocre eCE (positive and negative ΔT_{ad} of 1.8 K and 1.4 K, respectively, Fig. S5c). As the ordered domains fully transform into a Stream-like structure (Cu-18Zn-8Al-0.5V-0.3Si single-crystal alloy), the dominant martensite is the lath martensitic twins (Fig. S6). At this point, the role of the distortion region is mainly

https://doi.org/10.1038/s41467-025-65715-x

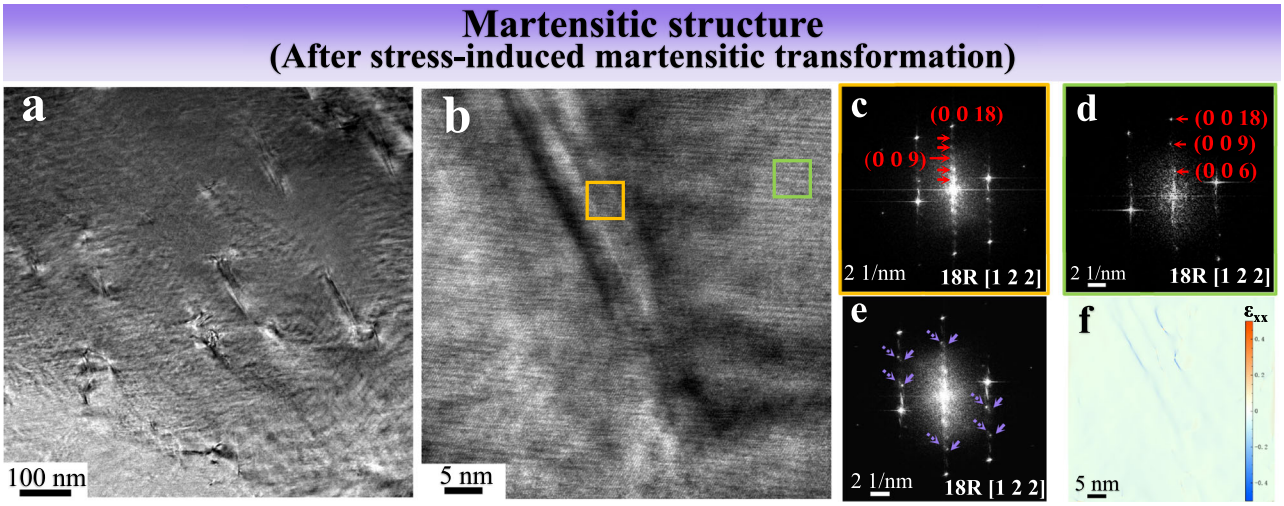

Fig. 5 | Microstructural changes after stress-induced martensitic transformation. a HRTEM image of Cu-18Zn-8Al-0.3V-0.3Si single-crystal alloy after deformation. **b** HRTEM image of the single martensitic lath and non-twinned martensite. **c**, **d** FFT results in orange and green boxes. **e** The corresponding FFT result of **b** shows diffraction spots belonging to a single martensite lath and another set from the non-twinned martensite, as indicated by the dashed and solid arrows, respectively. **f** The corresponding GPA result in (**b**).

to reduce the nucleation barrier, ultimately forming the lath martensitic twin group similar to conventional Cu-based sSMA. Consequently, the alloy exhibits a combination of low critical stress (~151.8 MPa) and severe stress hysteresis characteristics (Fig. S7a). Although it shows ideal eCE (positive and negative ΔT_{ad} of 5.1 K and 4.4 K, respectively, Fig. S7b), the additional dissipated work leads to a significant decrease in performance stability, with a cliff-like degradation in performance after only 48 cycles (Fig. S7c).

In conclusion, we have successfully prepared a highly efficient and stable Cu-18Zn-8Al-0.3V-0.3Si shape memory alloy for elastocaloric refrigeration materials. This material not only possesses an impressive recoverable strain of 13% but also exhibits low dissipated work, featuring a low stress hysteresis of approximately 8 MPa. Furthermore, it only requires a maximum driving force of 251.1 MPa to achieve the positive and negative ΔT_{ad} of 5.1 K and 4.4 K, respectively. It achieved a high COPmat value of 17.4 and maintained stability over 800 cycles. The elastocaloric cooling alloy has overcome the long-standing trade-off between strain-dissipated work and driving force-COP_{mat}.

The combination of characteristics stems from the special structures of the ordered domains and distortion regions caused by compositional modulation. The widespread 18 R long-period stacking order within the distortion regions not only reduces the martensite nucleation barrier but also provides favorable sites for nucleation, effectively reducing energy dissipation during the nucleation process. Numerous nucleation sites provide starting points for the growth of martensite, allowing it to expand rapidly at these locations without the need for long-range migration. Furthermore, under the influence of the single martensitic lath transformed from the dispersed ordered domains, the martensite within distortion regions can ultimately develop into the special structure of non-twinned martensite. Consequently, this significantly reduces the additional dissipation caused by phase boundary migration and internal friction at the phase interfaces. The highly efficient, high-performing, and stable cooling material holds significant potential for application in compact, energy-efficient, and highly reliable commercial refrigeration systems.

Methods

Cu-18Zn-8Al-0.3V-0.3Si, Cu-18Zn-8Al-0.3V-0.5Si, and Cu-18Zn-8Al-0.5V-0.3Si alloys (wt.%) were prepared in this study. The raw metals of Cu (99.9 wt.%), Zn (99.9 wt.%), Al (99.9 wt.%), V (99.9 wt.%), and Si (99.9 wt.%) were used. Firstly, the intermediate alloy with some part of Cu, Al, and all V/Si was fabricated by using arc melting in an argon environment. Subsequently, the obtained intermediate alloy and the rest of Cu, Al, and all Zn were sealed in a quartz tube, melted in a pit furnace at 1373 K, and then quenched in water to obtain cast alloys. The single-crystal alloys were obtained due to abnormal grain growth after annealing at 1023 K for 48 h.

Tensile specimens with 8 mm pitch and 2 mm width were cut from the single-crystal alloy using an electric spark wire cutting machine. Tensile tests at room temperature under different loading strains were conducted on Cu-18Zn-8Al-0.3V-0.3Si, Cu-18Zn-8Al-0.3V-0.5Si, and Cu-18Zn-8Al-0.5V-0.3Si single-crystal alloys using an electronic universal testing machine at a tensile rate of $4 \times 10^{-4}\,s^{-1}$. Furthermore, the Cu-18Zn-8Al-0.3V-0.3Si and Cu-18Zn-8Al-0.3V-0.5Si single-crystal alloys were both subjected to room temperature tensile cyclic tests. The former alloy underwent 400 cycles at an 8% strain, while the latter experienced 200 cycles at a 7% strain. The eCE cyclic stability tests were conducted under two distinct protocols: loading ($0.1\,s^{-1}$)—hold (12 s)—unloading ($0.1\,s^{-1}$)—hold (12 s), and loading ($0.1\,s^{-1}$)—unloading ($0.1\,s^{-1}$)—hold (10 s), with the hold time between loading and unloading omitted in the latter mode. The adiabatic temperature (ΔT_{ad}) was measured using a K-type thermocouple attached to the surface of the samples.

The microstructure and crystal structure of the samples were characterized by the transmission electron microscope (TEM) from FEI Talos F200X equipped with energy dispersive spectroscopy and selected area electron diffraction. The crystallographic orientation of the single-crystal was determined by electron backscatter diffraction. The reversible martensitic transformation temperatures were measured by differential scanning calorimetry with a rate of 10 K/min. The APT specimens were prepared using a dual-beam focused-ion-beam system and subsequently analyzed by a LEAP 5000 XR system (Cameca Instruments) in voltage pulsing mode.

https://doi.org/10.1038/s41467-025-65715-x

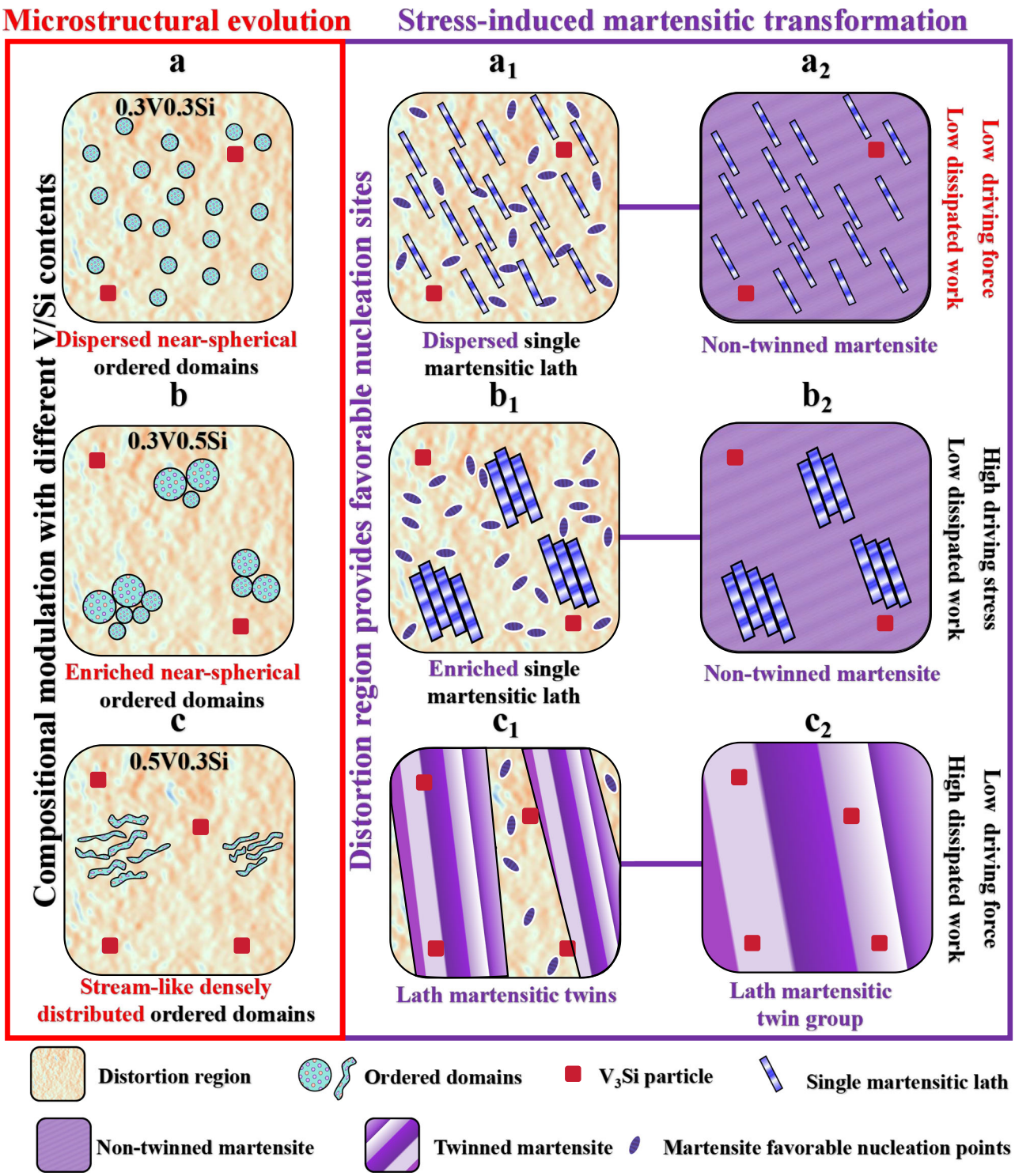

Fig. 6 | Microstructural evolution and stress-induced martensitic transformation mechanisms. Schematic diagram of the stress-induced martensitic transformation process in **a**–**a**$_2$ Cu-18Zn-8Al-0.3V-0.3Si, **b**–**b**$_2$ Cu-18Zn-8Al-0.3V-0.5Si, and **c**–**c**$_2$ Cu-18Zn-8Al-0.5V-0.3S single-crystal alloys.

Data availability

All data supporting the findings of this study are available within the main article, its Supplementary Information, and the accompanying Source data file. These include all processed data and raw values underlying the graphs and statistical analyses. No datasets were deposited in public repositories, as all relevant data are provided in the published materials. No custom code was used in this study. Source data are provided with this paper.

References

1. Dong, Y., Coleman, M. & Miller, S. A. Greenhouse gas emissions from air conditioning and refrigeration service expansion in developing countries. *Annu. Rev. Environ. Resour.* **46**, 59–83 (2021).
2. Mañosa, L. & Planes, A. Materials with giant mechanocaloric effects: cooling by strength. *Adv. Mater.* **29**, 1603607 (2017).
3. Bruederlin, F. et al. Elastocaloric cooling on the miniature scale: a review on materials and device engineering. *Energy Technol.* **6**, 1588–1604 (2018).

4. Moya, X. et al. Too cool to work. *Nat. Phys.* **11**, 202–205 (2015).
5. He, S. Y. et al. Accelerated learning and co-optimization of elastocaloric effect and stress hysteresis of elastocaloric alloys. *Rare Met.* **43**, 6606–6624 (2024).
6. Ossmer, H. et al. Local evolution of the elastocaloric effect in TiNi-based films. *Shape Mem. Superelasticity* **1**, 142–152 (2015).
7. Cui, J. et al. Demonstration of high efficiency elastocaloric cooling with large ΔT using NiTi wires. *Appl. Phys. Lett.* **101**, 073904 (2012).
8. Li, D. et al. Enhanced cyclability of elastocaloric effect in a directionally solidified $Ni_{55}Mn_{18}Ga_{26}Ti_1$ alloy with low hysteresis. *Scr. Mater.* **189**, 78–83 (2020).
9. Hou, H. et al. Fatigue-resistant high-performance elastocaloric materials made by additive manufacturing. *Science* **366**, 1116–1121 (2019).
10. Lin, H., Hua, P. & Sun, Q. Effects of grain size and partial amorphization on elastocaloric cooling performance of nanostructured NiTi. *Scr. Mater.* **209**, 114371 (2022).
11. Chen, J. et al. Toward tunable mechanical behavior and enhanced elastocaloric effect in NiTi alloy by gradient structure. *Acta Mater.* **226**, 117609 (2022).
12. Otsuka, K. & Ren, X. Physical metallurgy of Ti–Ni-based shape memory alloys. *Prog. Mater. Sci.* **50**, 511–678 (2005).
13. Tanaka, Y. et al. Ferrous polycrystalline shape-memory alloy showing huge superelasticity. *Science* **327**, 1488–1490 (2010).
14. Chen, H. et al. Unprecedented non-hysteretic superelasticity of [001]-oriented NiCoFeGa single crystals. *Nat. Mater.* **19**, 712–718 (2020).
15. Fu, Y. et al. Achieving large near-linear elasticity, low modulus, and high strength in a metastable β-Ti alloy by mild cold rolling. *J. Mater. Sci. Technol.* **189**, 1–12 (2024).
16. Hua, P. et al. Nanocomposite NiTi shape memory alloy with high strength and fatigue resistance. *Nat. Nanotechnol.* **16**, 409–413 (2021).
17. Imran, M. & Zhang, X. Recent developments on the cyclic stability in elastocaloric materials. *Mater. Des.* **195**, 109030 (2020).
18. Ma, J., Karaman, I. & Noebe, R. D. High temperature shape memory alloys. *Int. Mater. Rev.* **55**, 257–315 (2010).
19. Lu, N. H. & Chen, C. H. Compressive stress-induced martensitic transformation and elastocaloric effect in Cu-Al-Mn single-crystal alloy. *Mater. Sci. Eng. A* **840**, 142945 (2022).
20. Wang, Y. et al. Effect of burst-type martensitic transformation on superelastic and elastocaloric properties in a <116> oriented $Cu_{70.5}Al_{17.5}Mn_{12}$ single crystal. *Scr. Mater.* **246**, 116092 (2024).
21. Dang, P. et al. Improved stability of superelasticity and elastocaloric effect in Ti-Ni alloys by suppressing Lüders-like deformation under tensile load. *J. Mater. Sci. Technol.* **146**, 154–167 (2023).
22. Li, D. et al. Giant elastocaloric effect in Ni-Mn-Ga-based alloys boosted by a large lattice volume change upon the martensitic transformation. *ACS Appl. Mater. Interfaces* **14**, 1505–1518 (2022).
23. Xuan, H. et al. The effect of Co on elastocaloric and mechanical properties of Ni-Co-Mn-Al alloys. *Solid State Commun.* **301**, 113706 (2019).
24. Zhu, Y. et al. Large elastocaloric effect in as-cast Ni-Mn-Sn-Fe ferromagnetic shape memory alloys. *Phys. Lett. A* **451**, 128374 (2022).
25. Chen, J. et al. Improved elastocaloric cooling performance in gradient-structured NiTi alloy processed by localized laser surface annealing. *Acta Mater.* **208**, 116741 (2021).
26. Chen, H. et al. Stable and large superelasticity and elastocaloric effect in nanocrystalline Ti-44Ni-5Cu-1Al (at%) alloy. *Acta Mater.* **158**, 330–339 (2018).
27. Shen, J. J., Lu, N. H. & Chen, C. H. Mechanical and elastocaloric effect of aged Ni-rich TiNi shape memory alloy under load-controlled deformation. *Mater. Sci. Eng. A* **788**, 139554 (2020).
28. Ossmer, H. et al. Evolution of temperature profiles in TiNi films for elastocaloric cooling. *Acta Mater.* **81**, 9–20 (2014).
29. Ossmer, H., Miyazaki, S. & Kohl, M. The elastocaloric effect in TiNi-based Foils. *Mater. Today. Proc.* **2**, S971–S974 (2015).
30. Ulpiani, G. et al. Upscaling of SMA film-based elastocaloric cooling. *Appl. Therm. Eng.* **180**, 115867 (2020).
31. Zhang, K., Kang, G. & Sun, Q. High fatigue life and cooling efficiency of NiTi shape memory alloy under cyclic compression. *Scr. Mater.* **159**, 62–67 (2019).
32. Chen, J. et al. Ultra-high fatigue life of NiTi cylinders for compression-based elastocaloric cooling. *Appl. Phys. Lett.* **115**, 093902 (2019).
33. Chen, H. et al. Improvement of the stability of superelasticity and elastocaloric effect of a Ni-rich Ti-Ni alloy by precipitation and grain refinement. *Scr. Mater.* **162**, 230–234 (2019).
34. Kim, Y. et al. Elastocaloric effect in polycrystalline $Ni_{50}Ti_{45.3}V_{4.7}$ shape memory alloy. *Scr. Mater.* **144**, 48–51 (2018).
35. Eftifeeva, A. et al. Superelasticity and elastocaloric cooling capacity in stress-induced martensite aged [001]A-oriented $Ni_{54}Fe_{19}Ga_{27}$ single crystals. *Mater. Sci. Eng. A* **855**, 143855 (2022).
36. Imran, M. et al. Enhancing the elastocaloric cooling stability of Ni-Fe-Ga alloys via introducing pores. *Adv. Eng. Mater.* **22**, 1901140 (2020).
37. Xiao, F. et al. Elastocaloric effect in $Ni_{50}Fe_{19}Ga_{27}Co_4$ single crystals. *Acta Mater.* **96**, 292–300 (2015).
38. Panchenko, E. Y. et al. Elastocaloric effect in aged single crystals of $Ni_{54}Fe_{19}Ga_{27}$ ferromagnetic shape memory alloy. *Metals* **12**, 1398 (2022).
39. Yang, Z. et al. Large room-temperature elastocaloric effect in a bulk polycrystalline Ni-Ti-Cu-Co alloy with low isothermal stress hysteresis. *Appl. Mater. Today* **21**, 100844 (2020).
40. Chen, H. et al. Elastocaloric effect with a broad temperature window and low energy loss in a nanograin Ti-44Ni-5Cu-1Al (at.%) shape memory alloy. *Phys. Rev. Mater.* **5**, 015201 (2021).
41. Hou, R. et al. The role of texture on superelasticity and elastocaloric effect in severely rolled Ti-44Ni-5Cu-1Al (at%) shape memory alloy. *Scr. Mater.* **209**, 114334 (2022).
42. Chluba, C. et al. Ultra-low fatigue quaternary TiNi-based films for elastocaloric cooling. *Shape Mem. Superelasticity* **2**, 95–103 (2016).
43. Bumke, L. et al. Cu-rich $Ti_{52.8}Ni_{22.2}Cu_{22.5}Co_{2.5}$ shape memory alloy films with ultra-low fatigue for elastocaloric applications. *J. Appl. Phys.* **127**, 225105 (2020).
44. Schmidt, M., Schütze, A. & Seelecke, S. Elastocaloric cooling processes: the influence of material strain and strain rate on efficiency and temperature span. *APL Mater.* **4**, 064107 (2016).
45. Lu, B. et al. Reducing mechanical hysteresis via tuning the microstructural orientations in Heusler-type $Ni_{44.8}Mn_{36.9}In_{13.3}Co_{5.0}$ elastocaloric alloys. *J. Alloy. Compd.* **785**, 1023–1029 (2019).
46. Yang, Z. et al. Enhanced cyclability of elastocaloric effect in boron-microalloyed Ni-Mn-In magnetic shape memory alloys. *Acta Mater.* **127**, 33–42 (2017).
47. Wei, L. et al. Orientation dependent cyclic stability of the elastocaloric effect in textured Ni-Mn-Ga alloys. *AIP Adv.* **8**, 055312 (2018).
48. Mañosa, L. et al. Large temperature span and giant refrigerant capacity in elastocaloric Cu-Zn-Al shape memory alloys. *Appl. Phys. Lett.* **103**, 211904 (2013).
49. Wu, Y., Ertekin, E. & Sehitoglu, H. Elastocaloric cooling capacity of shape memory alloys – Role of deformation temperatures, mechanical cycling, stress hysteresis and inhomogeneity of transformation. *Acta Mater.* **135**, 158–176 (2017).
50. Wang, H., Huang, H. & Xie, J. Effects of strain rate and measuring temperature on the elastocaloric cooling in a columnar-grained $Cu_{71}Al_{17.5}Mn_{11.5}$ shape memory alloy. *Metals* **7**, 527 (2017).
51. Qian, S. et al. Elastocaloric effect in CuAlZn and CuAlMn shape memory alloys under compression. *Philos. T. R. Soc. A* **374**, 20150309 (2016).

52. Xiao, F., Fukuda, T. & Kakeshita, T. Significant elastocaloric effect in a Fe-31.2Pd (at. %) single crystal. *Appl. Phys. Lett.* **102**, 161914 (2013).

Acknowledgements

This work was supported by the National Natural Science Foundation of China (Grant No. 52471209) and the Shenzhen Science and Technology Program (Grant No. JCYJ20210324121800001), both awarded to S.Y.

Author contributions

S.Y. Yang, C.P. Wang, and X.J. Liu conceived and designed the experiments. L.S. Wang, X.Y. Qing, and L.P. Guo prepared the samples and performed electrical resistivity experiments. J.H. Mei and L.P. Guo performed image processing of TEM and APT results. J.H. Mei and F. Xiao performed a tensile test on the samples. J.H. Mei and S.Y. Yang assisted in the research and discussion. J.H. Mei and S.Y. Yang wrote the paper, and all authors discussed the results and commented on the manuscript.

Competing interests

The authors declare no competing interests.

Additional information

Supplementary information The online version contains supplementary material available at https://doi.org/10.1038/s41467-025-65715-x.

Correspondence and requests for materials should be addressed to Cuiping Wang or Shuiyuan Yang.

Peer review information *Nature Communications* thanks Jun Cui and the other anonymous reviewer(s) for their contribution to the peer review of this work. A peer review file is available.

Reprints and permissions information is available at http://www.nature.com/reprints

Publisher's note Springer Nature remains neutral with regard to jurisdictional claims in published maps and institutional affiliations.

Open Access This article is licensed under a Creative Commons Attribution-NonCommercial-NoDerivatives 4.0 International License, which permits any non-commercial use, sharing, distribution and reproduction in any medium or format, as long as you give appropriate credit to the original author(s) and the source, provide a link to the Creative Commons licence, and indicate if you modified the licensed material. You do not have permission under this licence to share adapted material derived from this article or parts of it. The images or other third party material in this article are included in the article's Creative Commons licence, unless indicated otherwise in a credit line to the material. If material is not included in the article's Creative Commons licence and your intended use is not permitted by statutory regulation or exceeds the permitted use, you will need to obtain permission directly from the copyright holder. To view a copy of this licence, visit http://creativecommons.org/licenses/by-nc-nd/4.0/.

© The Author(s) 2025